Influence of Rigidity-Hydration Coupling on Size-Dependent Diffusion in Hydrated Polymer Membranes

Paul R. Irving, Soham Rane, Benny D. Freeman,* and Venkat Ganesan*

Department of Chemical Engineering, University of Texas at Austin

E-mail: freeman@che.utexas.edu; venkat@che.utexas.edu

Abstract

Selective ion transport in polymer membranes depends critically on how penetrant motion couples to polymer dynamics and hydration. Yet, the mechanistic interplay between polymer rigidity, water content, and penetrant size remains poorly understood, especially in the regime where the penetrant diameter, polymer Kuhn length, and correlation length are comparable. Here, we employ coarse-grained molecular dynamics simulations to systematically investigate penetrant diffusion in hydrated polymer networks across a broad range of water volume fractions, chain rigidities, and penetrant sizes. The results reveal a transition from a decoupled regime, where small penetrants diffuse nearly independently of polymer relaxation, to a coupled regime in which large penetrants require cooperative polymer motion for transport. Increasing polymer rigidity amplifies the sensitivity of diffusivity to hydration, particularly at low water contents, leading to pronounced deviations from Stokes–Einstein scaling. Comparison with scaling theories and free-volume models shows that classical nanoparticle-based frameworks fail to capture this intermediate regime. To address this gap, we extend the Yasuda model to incorporate polymer rigidity through a single parameter that quantifies the dynamic contribution of chain stiffness to free-volume fluctuations. The resulting model collapses diffusivity data across all sizes, water contents, and rigidities, providing a unified description of penetrant transport in hydrated polymer matrices. These findings establish polymer rigidity as a key, tunable determinant of diffusion and offer a framework for interpreting size-dependent transport in ion-selective membranes.

Membrane-based separations underpin a vast range of technologies, from water purification and gas separations to emerging applications in energy and resource recovery.[1,2] Their scalability, modularity, and low energy demand have made them indispensable for sustainable chemical processing. Yet, as the field moves toward increasingly demanding separations such as lithium extraction,[3] rare-earth element purification,[4] and water softening,[5] the fundamental challenge has shifted: membranes must now discriminate between ions that are nearly indistinguishable in size and charge.[6] Achieving such fine selectivity requires not only precise chemical design but also a deep understanding of how nanoscale polymer dynamics govern ion and molecule transport under confinement.[5]

Despite decades of progress, the physical principles linking polymer structure to selective transport remain poorly understood.[7] Traditional design frameworks often treat water content as the dominant control parameter, assuming that diffusivity scales primarily with solvent-swollen free volume.[8,9] However, emerging experimental and computational studies, including our recent work,[10–14] demonstrate that polymer dynamics, particularly backbone rigidity, play an equally important yet often overlooked role. In hydrated membranes, rigidity modulates both the amplitude and timescale of local free-volume fluctuations, thereby altering the effective mobility landscape experienced by the diffusing species. In a recent work, we showed that lithium–magnesium selectivity in hydrated polymer membranes can be tuned by controlling both chain rigidity and water content, with the observed selectivity arising primarily from differences in ion diffusivity rather than sorption.[10] In particular, magnesium transport exhibited stronger sensitivity to polymer relaxation and swelling at low hydration levels.

However, this raises a deeper question: are there intrinsic limits to stiffness-induced selectivity? At what point does increasing rigidity no longer enhance discrimination, but instead suppresses mobility for all species? Addressing these questions requires moving beyond the classical view that water content alone governs transport. Classical transport models, including those of Yasuda and Mackie–Meares, neglect polymer segmental dynamics entirely,[8,9] while free-volume and cooperative relaxation theories capture such effects only through empirical fitting.[15–17] Scaling theories developed for nanoparticle diffusion have provided valuable insight into coupled and decoupled transport regimes, but they fail to describe the intermediate regime most relevant to ion and small-molecule transport.[18,19] Indeed, while nanoparticles typically satisfy the condition $b \ll d \sim \xi$ (where b is the Kuhn length, d is the particle diameter, and ξ is the correlation length), (hydrated) ions more commonly fall within the regime $d \sim b$.[20,21]

The central question motivating this work is: how does polymer rigidity set both the magnitude and the limit of size- and hydration-based selectivity in hydrated membranes? By establishing a unified framework that connects polymer stiffness, hydration, and size-dependent diffusivity, we aim to identify when rigidity enhances selectivity, and when it simply arrests transport. To systematically investigate how penetrant size, polymer rigidity, and water content influence diffusion in this regime ($d \sim b \sim \xi$), we conducted a series of coarse-grained molecular dynamics (CGMD) simulations. CGMD offers a computationally efficient framework for probing transport behavior across a broad parameter space under well-controlled conditions.[22] In this study, we employed CGMD simulations to systematically probe how polymer rigidity, hydration, and penetrant size govern diffusive transport in hydrated polymer networks. In contrast to our previous simulations, which incorporated explicit ion–ion electrostatics and solvent-specific interactions to capture hydration effects,[10] the present study focuses on simplified, neutral penetrants of varying size. By holding Lennard-Jones interaction parameters constant across penetrant species and systematically tuning backbone stiffness and hydration, we isolate the effect of polymer rigidity and excluded-volume interactions while eliminating ambiguities associated with defining ion size in the presence of strong hydration. For this study, we also restrict ourselves to systems with relatively homogeneous water distributions, therefore our conclusions may not apply to materials with phase-separated morphologies. This minimalistic approach enables direct mapping of the transition from decoupled, solvent-dominated diffusion to coupled, polymer-governed transport. The resulting scaling behavior exposes the breakdown of classical models and establishes a unified framework connecting polymer rigidity, hydration, and penetrant mobility, therefore offering new molecular-level insight into how polymer structure encodes selectivity in hydrated membranes.

Simulation systems comprised linear polymer chains, solvent beads, and penetrant particles, as illustrated in Figure 1A. All simulations were performed using the GROMACS 2020.5 package,[23–30] and methodological details are provided in the Supporting Information. Polymer backbone stiffness was varied through the harmonic bond angle interaction:

$$U_\theta = \frac{k_\theta}{2}(\theta - \theta_0)^2 \tag{1}$$

where θ is the angle formed by three consecutive monomer beads, θ_0 is the equilibrium angle, and k_θ is the angular force constant. Increasing k_θ produces progressively more rigid chains. Representative snapshots (Figure 1A) show homogeneous distributions of polymer and solvent beads, consistent with θ-solvent conditions imposed by the Lennard-Jones interactions. Larger values of k_θ correspond to more rigid polymer chains (i.e. larger Kuhn segment lengths), as shown in the Supporting Information in Figure S8A.

Our simulation results (Figure 1B) indicate that penetrant diffusivities depend strongly on polymer rigidity, hydration, and penetrant size, with these variables exhibiting pronounced nonlinear coupling. As expected, diffusivity increased with higher water content, smaller penetrant size, and lower polymer rigidity. Yet these effects were not independent: rigidity had little influence on small penetrants but became dominant for larger ones in low-hydration environments, while water content strongly affected large penetrants but had minimal impact on small ones. The distinction between these transport regimes is clearest for the smallest penetrants ($d = 0.25\sigma$, where σ is the Lennard-Jones diameter of polymer and solvent beads), whose diffusivities—shown in Figures S6—collapse onto those in pure solvent, indicating motion through transient solvent-sized voids that form independently of polymer rigidity. By contrast, for larger penetrants ($d \geq 0.5\sigma$), the diffusivity decreases with increasing rigidity and decreasing water content; the corresponding curves in Figure 1B diverge substantially, revealing strong coupling between penetrant motion and polymer dynamics. This rigidity- and hydration-dependent behavior marks a size-dependent crossover from solvent-controlled to polymer-controlled transport, where diffusion requires cooperative relaxation events of the polymer matrix.

At high water contents, where polymer contributions are expected to be minimal, diffusivity is expected to follow the classical Stokes–Einstein scaling:

$$D_w = \frac{k_B T}{3\pi\eta_s d} \tag{2}$$

where D_w is the penetrant diffusivity in solvent (i.e., no polymer), k_B is the Boltzmann constant, T is the absolute temperature, η_s is the solvent viscosity, and d is the penetrant diameter. As shown in Figure S1 in the Supporting Information, our simulation results for polymer-free systems are consistent with the Stokes-Einstein relationship, with $\log D$ vs. $\log(d)$ being linear with a slope of $\simeq -1.10$. In contrast, in polymer melts and poorly hydrated matrices, the scaling becomes steeper ($\log D \sim -1.62 \log d$ for flexible chains and up to $-3.12 \log d$ for rigid chains), indicating a breakdown of hydrodynamic behavior. These deviations indicate that in dense or rigid matrices, penetrant motion is governed not by viscous drag but by cooperative segmental relaxation of the polymer network.

To interpret the above deviations, we first compare our data with the scaling theory

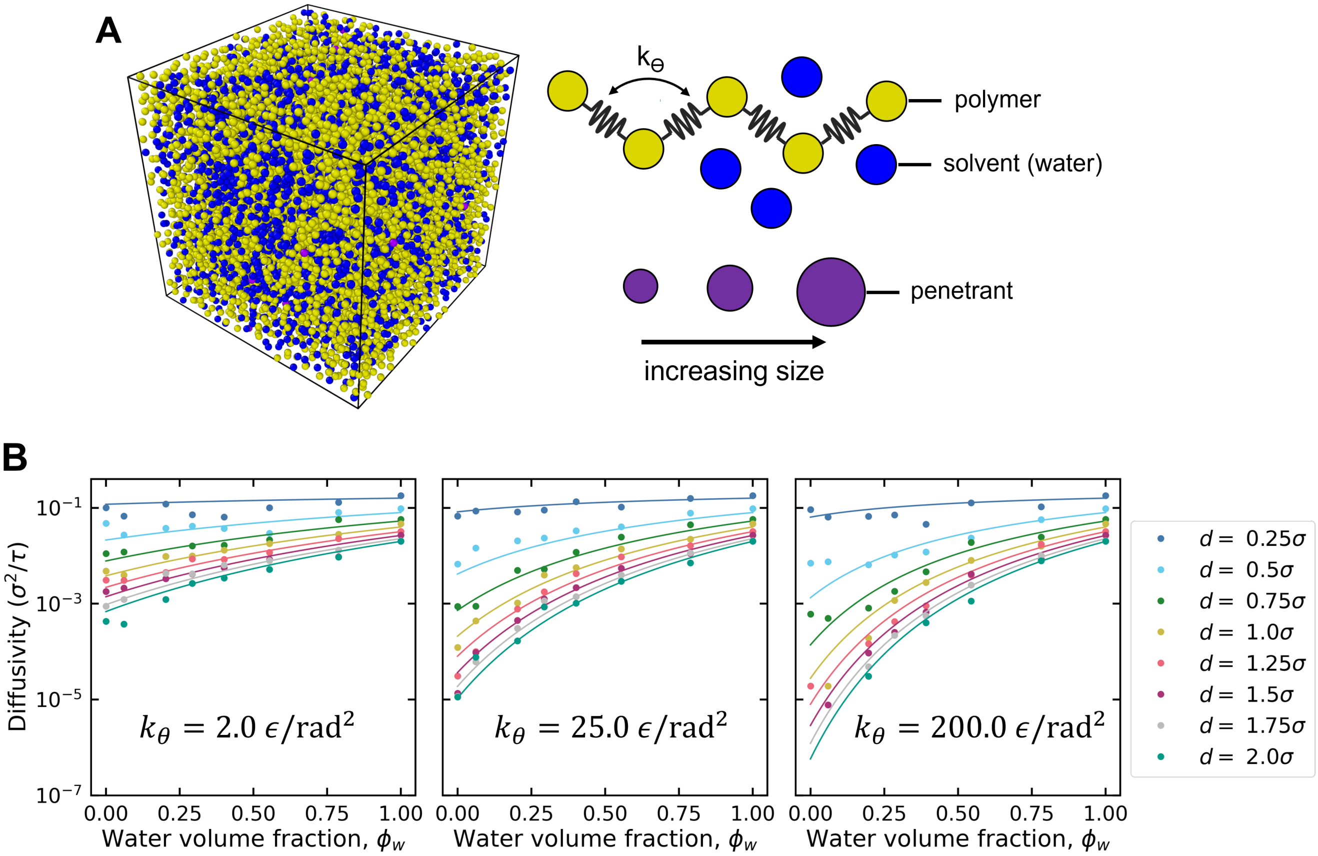

Figure 1: (A) Coarse-grained molecular dynamics simulation box snapshot (nominal water volume fraction of 0.35, a k_θ-value of $25.0\epsilon/\mathrm{rad}^2$, and penetrant diameter of 1σ). Yellow, blue, and purple correspond to polymer, water, and penetrant beads, respectively. While the cartoon shows a polymer with 5 monomer beads, simulated chains consist of 50 monomer beads to reduce end effects. (B) Penetrant diffusivity vs. membrane water volume fraction for a subset of k_θ-values (2.0, 25.0, $200.0\epsilon/\mathrm{rad}^2$). Similar plots for the remaining seven k_θ-values are provided in the Supporting Information in Figure S7. Lines represent a fit to Equations 7 and 8. The following parameters were used for the fits: $D_0 = 0.1944\sigma^2/\tau$, $d_0 = 0.2049\sigma$, $B = 1.563$, $\alpha_{2.0} = 0.6339$, $\alpha_{25.0} = 0.4364$, $\alpha_{200.0} = 0.3585$.

developed by Cai *et al.*,[18] which distinguishes between $d < \xi$ and $d > \xi$ regimes:

$$D \approx \begin{cases} \frac{k_B T}{\eta_s d} & , d < \xi \\ \frac{k_B T \xi^2}{\eta_s d^3} & , d > \xi \end{cases} \tag{3}$$

where ξ is the correlation length of the polymer solution. We directly calculated ξ from pore-size distributions,[31] which are provided in Figure S2A and B. As shown in Figure S2C, $\log \xi$ vs. $\log \phi_p$ (where ϕ_p is the polymer volume fraction) demonstrated a slope of -1.15, roughly consistent with theory which predicts a slope of -1 in θ-solvent.[32]

Following Chen et al.,[18,33] we assessed the applicability of the above scaling model by plotting D/D_w versus d/ξ for simulation data with varying polymer flexibility, water content, and penetrant diameter. The theory predicts a plateau ($D/D_w \approx 1$) for $d/\xi < 1$, corresponding to solvent-like diffusion, and a steep decay with slope –2 for $d/\xi > 1$, where polymer constraints dominate. As shown in Figure 2A, our data qualitatively reproduce the existence of a crossover but diverge quantitatively from theoretical expectations. The transition occurs at smaller d/ξ than predicted, and the apparent slope in the polymer-dominated regime differs from –2, particularly for systems with rigid chains. Moreover, increasing chain rigidity amplifies the dependence of D/D_w on d/ξ, producing an expanded separation among curves that is absent in flexible systems. These trends confirm that while the Cai model captures the overall crossover, it fails to account for the critical role of polymer rigidity and the dynamic nature of free-volume fluctuations in dense networks.

We attribute the discrepancy between our simulations and the Cai model to the fact that our penetrants are much smaller than the "nanoparticle limit" for which the theory was derived. In the nanoparticle regime, particle diameters and polymer correlation lengths exceed the Kuhn length (d, $\xi > b$). Diffusion in this regime is governed primarily by the particle's coupling to the collective motion and hydrodynamic drag of the correlation blobs, rather than by local segmental dynamics. Because the particle averages over many Kuhn segments, the influence of microscopic features such as chain stiffness is effectively averaged

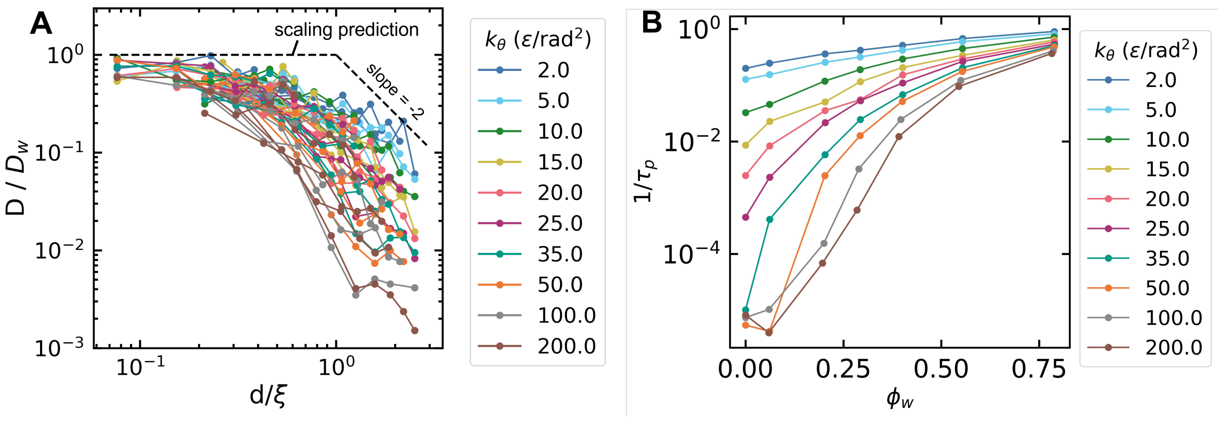

Figure 2: (A) Comparison of simulated diffusivity data (for variable polymer flexibility, water content, and penetrant diameter) with scaling prediction from Equation 3.[18,33] (B) Inverse of the polymer relaxation timescale, τ_p, vs. water volume fraction for polymers of varying backbone flexibility. The relaxation timescale is strongly coupled to both water content and polymer flexibility at low water volume fractions.

out.

In contrast, in our simulations the penetrant size is comparable to both the Kuhn length and the correlation length ($d \sim b \sim \xi$), where transport couples simultaneously to hydrodynamic interactions and segmental relaxation dynamics. In this intermediate regime, motion depends on transient free volume generated by local conformational fluctuations of the chains. Consequently, diffusivity becomes highly sensitive to both polymer rigidity and hydration. This coupling is evident in the steepening of the $\log D$ versus $\log d$ slope with increasing stiffness (Figure S1), reflecting the influence of chain relaxation timescales on transport. The same trend appears in polymer relaxation times extracted from segmental orientation correlations (Figure 2B), which become longer with increasing rigidity and decreasing hydration. Together, these results indicate that when $d \sim b \sim \xi$, penetrant motion is governed by segmental relaxation processes not captured by nanoparticle theories such as those of Cai *et al.*

The size-dependent crossover from solvent- to polymer-controlled transport revealed in our simulations motivates the development of a unified framework capable of capturing both regimes within a single description. We begin by extending the classical free-volume model of Yasuda et al.:[34]

$$D = D_w \exp\left(\frac{\beta\left(\alpha-1\right)\left(1-\phi_w\right)}{\phi_w+\alpha\left(1-\phi_w\right)}\right) \tag{4}$$

where ϕ_w is the water volume fraction in the polymer/solvent mixture, α and β are given as:

$$\alpha = V_{f,p}/V_{f,w} \tag{5}$$

$$\beta = V^*/V_{f,w} \tag{6}$$

where $V_{f,p}$ is the polymer fractional free volume, $V_{f,w}$ is the water fractional free volume, and V^* is a parameter with strong dependence on penetrant size (often assumed to be proportional to the penetrant cross-sectional area times the diffusion jump distance).[35] In the original formulation, α is a polymer-specific parameter and β reflects penetrant size. However, as detailed in the Supporting Information, direct evaluation of free volume from simulations does not provide reliable values of α; fractional free volume depends only weakly on polymer backbone dynamics, and more rigid polymers can even exhibit slightly higher free volume. Motivated by these observations, we modify the Yasuda model based on 3 physical details. First, transport is governed by the formation of transient pathways whose rate is set by polymer relaxation, so increasing rigidity suppresses diffusivity even when the average free volume does not decrease, indicating that α reflects dynamical constraints rather than static free volume. Second, we account for the decoupling of solute mobility from polymer dynamics for sufficiently small penetrants by assuming that particles of diameter, d_0, diffuse with a reference diffusivity, D_0, independent of rigidity or hydration. Third, matching the Yasuda form to the observed $\log D \sim \log d$ scaling requires the activation term to vary as $\ln(d/d_0)$ rather than with penetrant volume. This leads naturally to redefining $\beta \propto \ln(d/d_0)$ and yields the following form (see pages S13-S14 in the SI for more details):

$$\frac{D}{D_0} = \left(\frac{d_0}{d}\right)^{\gamma} \tag{7}$$

where γ is given as:

$$\gamma = \frac{1 + B(1-\phi_w)(1-\alpha)}{\phi_w + \alpha(1-\phi_w)} \tag{8}$$

where α decreases with increasing chain rigidity and B is a constant independent of polymer rigidity, hydration, or penetrant size.

We fit Equations 7 and 8 to diffusivity data to yield values for D_0, d_0, B, and α. The α-values were allowed to vary only with polymer rigidity (k_θ), while D_0, d_0, and B were held constant regardless of rigidity, water content, or penetrant size. Therefore for our simulation data, there are a total of 13 fitting parameters (one for each of the 10 unique α-values, 1 B-value, 1 d_0-value, and 1 D_0-value). With the exception of B, each parameter has a precise physical interpretation. The α parameters represent the rigidity of the polymer, d_0 is a sufficiently small size such that the diffusivity, D_0, is equal for all polymer rigidities and solvent contents. It is encouraging that the computed values of α display a monotonic dependence on rigidity (inset of Figure 3A). A parity plot for the fit is provided in Figure 3B, demonstrating an R^2 of 0.977. By assuming some empirical relation for α vs. k_θ or α vs. b, the number of parameters can be decreased significantly. As shown in Figure S8, the relationship between $\log \alpha$ and Kuhn length is approximately linear, suggesting the following empirical relationship:

$$\alpha = k_2 e^{-k_1 b} \tag{9}$$

where k_1 and k_2 are adjustable parameters. By incorporating Equation 9, the number of fitting parameters for the entire diffusivity dataset can be reduced to 5 (D_0, d_0, B, k_1 and k_2). As shown in Figures S9, such a procedure also provides good fit to simulation data, with $R^2 = 0.968$.

Fits to Equations 7 and 8 for a subset of k_θ-values are provided in Figure 1B. As shown, the fitted curves show good agreement with the simulation data. In Figure 3, we plot D/D_0 vs. $\gamma = \frac{1+B(1-\phi_w)(1-\alpha)}{\phi_w+\alpha(1-\phi_w)}$ which causes points with different rigidity and water content to collapse onto a unique curve for each penetrant diameter. As shown, small penetrants are decoupled from polymer and water dynamics, showing very weak dependence on γ, while larger penetrants are more significantly affected.

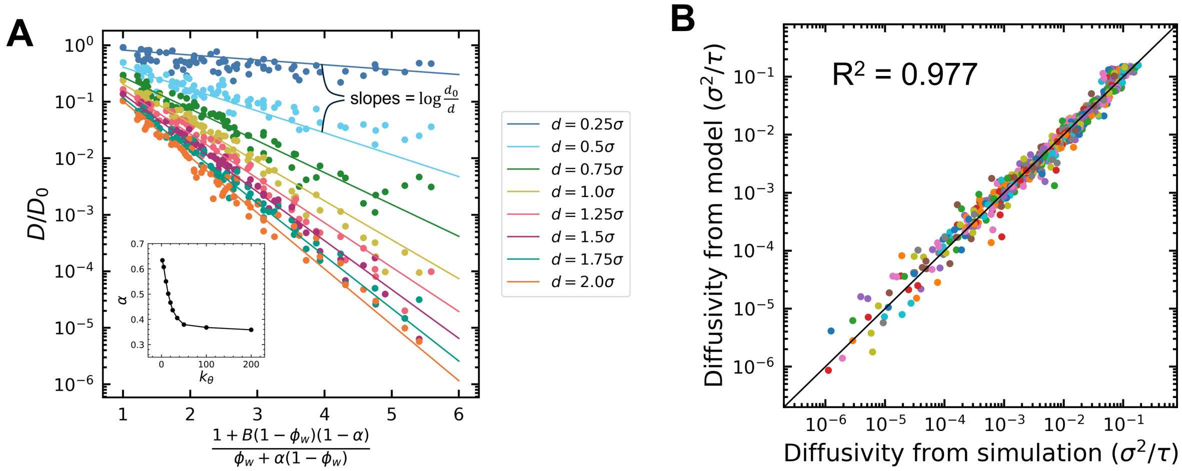

Figure 3: (A) Normalized diffusivity vs. $\gamma = (1 + B(1-\phi_w)(1-\alpha))/(\phi_w + \alpha(1-\phi_w))$ allows for collapse of diffusivity data onto universal curves for each penetrant diameter. (B) Parity plots of modeled vs. simulated diffusivity for the fit to Equations 7 and 8.

Overall, the model not only provides a good fit to the simulation data but also offers physical insight into how polymer dynamics and water content jointly control penetrant transport. By explicitly incorporating chain rigidity through the parameter α, the model captures how increased stiffness amplifies the sensitivity of diffusivity to hydration, particularly for larger penetrants. Likewise, the collapse of data when plotted against γ highlights that water content and rigidity do not act independently, but instead combine to set an effective free-volume landscape that governs transport. In this framework, small penetrants diffuse in a manner largely decoupled from polymer relaxation, while larger penetrants experience progressively stronger coupling to both water volume fraction and chain rigidity. Mechanistically, the model suggests that hydration controls the amount of accessible free volume, while polymer rigidity dictates how that free volume is dynamically reconfigured, together defining the scaling of penetrant diffusivity with penetrant size across regimes.

In Figures 4A and B, we evaluate the implications of Equations 7 and 8 on membrane separation performance. As shown in Figure 4A, the model predicts an increase in diffusion selectivity with increasing polymer rigidity, as supported by our experimental work.[10] However, in the extreme of a very rigid polymer ($\alpha \to 0$), further increase of polymer rigidity has a minimal effect on improving selectivity. Rather, it appears that rigid polymers and extremely rigid polymers have similar separation performance. In Figure 4B, we evaluate predicted membrane separation performance and the permeability-selectivity tradeoff, where we assume that the membrane phase sorption coefficients are equal to the water volume fraction (i.e., penetrants dissolve only in the water phase of the membrane). This approximation assumes that the sorption selectivity in the membrane is always equal to 1.0. As shown, an increase in polymer rigidity tends to move materials to the upper right hand quadrant, suggesting an improvement in separation performance, as was also observed experimentally.[10] We expect these design rules to apply to materials with relatively uniform hydration structure. Materials with significant polymer/water phase separation may have interconnected water channels, shifting performance to the solvent-dominated Stokes-Einstein regime.

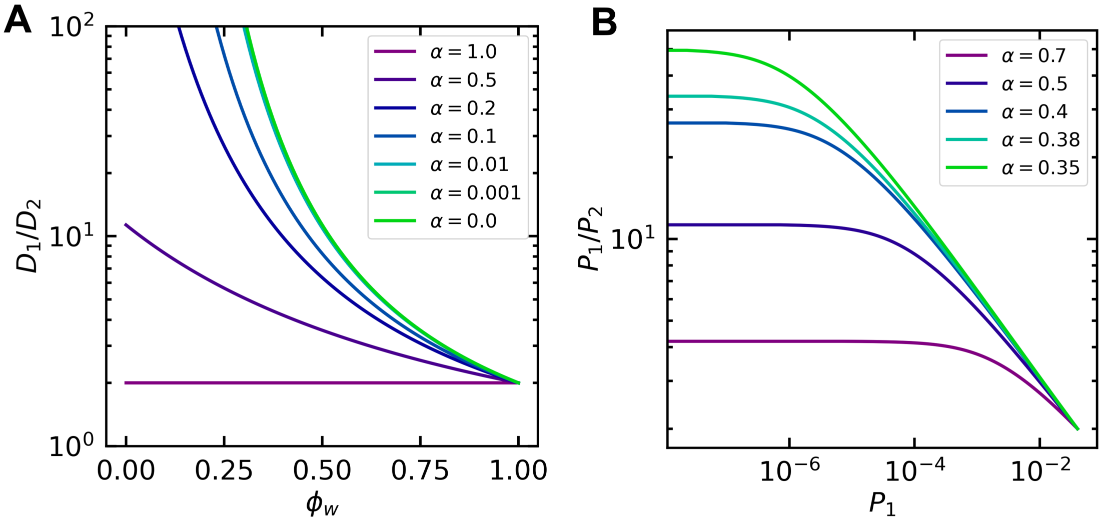

Figure 4: (A) Model predictions using Equations 7 and 8 demonstrate an increase in selectivity with increasing rigidity, up to a certain point, beyond which increasing rigidity has a diminishing effect on selectivity. (B) Model prediction of the permeability-selectivity tradeoff assuming sorption coefficients, K_i, are equal to the water volume fraction. As shown, performance improves with increasing polymer rigidity. Predictions used the following values: $d_0 = 0.2\sigma$, $D_0 = 0.2\sigma^2/\tau$, $d_1 = 1\sigma$, $d_2 = 2\sigma$, $B = 1.5$. D_1 and D_2 correspond to the diffusivity values of penetrants with diameters d_1 and d_2, respectively. P_1 and P_2 are the corresponding permeabilities, assuming $P_i = K_i D_i$.

To conclude, we have evaluated how the interplay between penetrant size, polymer rigidity, and polymer swelling affect penetrant diffusivity in hydrated membrane systems. For very small penetrants, diffusivity is decoupled from both solvent content and polymer dynamics. For highly hydrated systems, diffusivity follows the Stokes-Einstein relationship. However, when penetrant size is large and water content is low, polymer dynamics, water content, and penetrant size each have important impacts on penetrant diffusivity. Since Kuhn length, penetrant diameter, and polymer correlation length are all of similar size, the underlying physics is complex. Unlike the highly swollen case, polymer dynamics on the Kuhn-scale show strong dependence on both solvent content and the polymer rigidity, not accounted for in traditional scaling-models. Free-volume based approaches appear to fit penetrant diffusivity data adequately. Relaxation of polymer segments is therefore expected to occur through the same mechanism. From a materials design perspective, our results suggest that by designing materials with homogeneous water distribution and low to moderate water volume fraction (such that $d \sim \xi$), selectivity between penetrants with diameter on the Kuhn-scale ($d \sim b$) can be optimized by increasing polymer rigidity. These design rules show promise for emerging applications such as lithium extraction, rare-earth element purification, and the design of redox flow batteries.

Acknowledgement

This work was supported as part of the Center for Materials for Water and Energy Systems (M-WET), an Energy Frontier Research Center funded by the U.S. Department of Energy, Office of Science, Basic Energy Sciences, under Award #DE-SC0019272. The results in this paper were generated using high-performance computing resources provided by The University of Texas at Austin Texas Advanced Computing Center.

Supporting Information Available

Simulation methods, pore size distributions, polymer relaxation timescales, diffusivity model derivation, and comparison of simulation data with several diffusivity models.

References

(1) Baker, R. W. *Membrane Technology and Applications*; John Wiley & Sons, 2012.

(2) Sholl, D. S.; Lively, R. P. Seven chemical separations to change the world. *Nature* **2016**, *532*, 435–437.

(3) Li, X.; Mo, Y.; Qing, W.; Shao, S.; Tang, C. Y.; Li, J. Membrane-based technologies for lithium recovery from water lithium resources: A review. *J. Membr. Sci.* **2019**, *591*, 117317.

(4) Elbashier, E.; Mussa, A.; Hafiz, M.; Hawari, A. H. Recovery of rare earth elements from waste streams using membrane processes: An overview. *Hydrometallurgy* **2021**, *204*, 105706.

(5) Tang, C.; Bruening, M. L. Ion separations with membranes. *J. Polym. Sci.* **2020**, *58*, 2831–2856.

(6) DuChanois, R. M.; Porter, C. J.; Violet, C.; Verduzco, R.; Elimelech, M. Membrane materials for selective ion separations at the water–energy nexus. *Adv. Mater.* **2021**, *33*, 2101312.

(7) Geise, G. M.; Paul, D. R.; Freeman, B. D. Fundamental water and salt transport properties of polymeric materials. *Prog. Polym. Sci.* **2014**, *39*, 1–42.

(8) Mackie, J.; Meares, P. The diffusion of electrolytes in a cation-exchange resin membrane I. Theoretical. *Proc. R. Soc. Lond. A: Math. Phys. Eng. Sci.* **1955**, *232*, 498–509.

(9) Yasuda, H.; Lamaze, C.; Ikenberry, L. Permeability of solutes through hydrated polymer membranes. *Makromol. Chem.* **1968**, *118*, 19–35.

(10) Irving, P. R.; Sam, G.; Rane, S.; Thirumalai, N.; Marioni, N.; Geise, G. M.; Freeman, B. D.; Ganesan, V. Engineering lithium–magnesium selectivity in hydrated polymer membranes through polymer backbone rigidity. *ACS Macro Lett.* **2025**, *14*, 161–168.

(11) Irving, P. R.; Reimund, K. K.; Zofchak, E. S.; Marioni, N.; Freeman, B. D.; Ganesan, V. Cellulose acetate membranes exhibit exceptional monovalent to divalent cation selectivities. *J. Membr. Sci.* **2024**, *706*, 122892.

(12) Chang, K.; Xue, T.; Geise, G. M. Increasing salt size selectivity in low water content polymers via polymer backbone dynamics. *J. Membr. Sci.* **2018**, *552*, 43–50.

(13) Chang, K.; Korovich, A.; Xue, T.; Morris, W. A.; Madsen, L. A.; Geise, G. M. Influence of rubbery versus glassy backbone dynamics on multiscale transport in polymer membranes. *Macromolecules* **2018**, *51*, 9222–9233.

(14) Korovich, A. G.; Chang, K.; Geise, G. M.; Madsen, L. A. Local water transport in rubbery versus glassy separation membranes and analogous solutions. *Macromolecules* **2021**, *54*, 11187–11197.

(15) Vrentas, J. S.; Duda, J. L. Diffusion in polymer—solvent systems. I. Reexamination of the free-volume theory. *J. Polym. Sci.* **1977**, *15*, 403–416.

(16) Mirigian, S.; Schweizer, K. S. Elastically cooperative activated barrier hopping theory of relaxation in viscous fluids.I.General formulation and application to hard sphere fluids. *J. Chem. Phys.* **2014**, *140*, 194506.

(17) Mei, B.; Lin, T.-W.; Sheridan, G. S.; Evans, C. M.; Sing, C. E.; Schweizer, K. S.

How segmental dynamics and mesh confinement determine the selective diffusivity of molecules in cross-linked dense polymer networks. *ACS Cent. Sci.* **2023**, *9*, 508–518.

(18) Cai, L.-H.; Panyukov, S.; Rubinstein, M. Mobility of nonsticky nanoparticles in polymer liquids. *Macromolecules* **2011**, *44*, 7853–7863.

(19) Cai, L.-H.; Panyukov, S.; Rubinstein, M. Hopping diffusion of nanoparticles in polymer matrices. *Macromolecules* **2015**, *48*, 847–862.

(20) Nightingale, E. R. Phenomenological theory of ion solvation. Effective radii of hydrated ions. *J. Phys. Chem.* **1959**, *63*, 1381–1387.

(21) Fetters, L. J.; Lohse, D. J.; Colby, R. H. In *Physical Properties of Polymers Handbook*; Mark, J. E., Ed.; Springer New York: New York, NY, 2007; pp 447–454.

(22) Shen, K.-H.; Fan, M.; Hall, L. M. Molecular dynamics simulations of ion-containing polymers using generic coarse-grained models. *Macromolecules* **2021**, *54*, 2031–2052.

(23) Bekker, H.; Berendsen, H.; Dijkstra, E.; Achterop, S.; Drunen, R.; Spoel, D.; Sijbers, A.; Keegstra, H. In *Physics Computing 92*; Groot, R., Nadrchal, J., Eds.; 1993; p 252–256.

(24) Berendsen, H.; Spoel, D.; Drunen, R. GROMACS: A message-passing parallel molecular dynamics implementation. *Comput. Phys. Commun.* **1995**, *91*, 43–56.

(25) Lindahl, E.; Hess, B.; Spoel, D. GROMACS 3.0: A package for molecular simulation and trajectory analysis. *J. Mol. Model.* **2001**, *7*, 306–317.

(26) Spoel, D.; Lindahl, E.; Hess, B.; Groenhof, G.; Mark, A.; Berendsen, H. GROMACS: Fast, flexible and free. *J. Comp. Chem.* **2005**, *26*, 1701–1718.

(27) Hess, B.; Kutzner, C.; Spoel, D.; Lindahl, E. GROMACS 4: Algorithms for highly efficient, load-balanced, and scalable molecular simulation. *J. Chem. Theory Comput.* **2008**, *4*, 435–447.

(28) Pronk, S.; Páll, S.; Schulz, R.; Larsson, P.; Bjelkmar, P.; Apostolov, R.; Shirts, M.; Smith, J. GROMACS 4.5: A high-throughput and highly parallel open source molecular simulation toolkit. *Bioinformatics* **2013**, *29*, 845–854.

(29) Páll, S.; Abraham, M.; Kutzner, C.; Hess, B.; Lindahl, E. In *Solving software challenges for exascale*; Markidis, S., Laure, E., Eds.; Springer International Publishing Switzerland: London, 2015; p 3–27.

(30) Abraham, M.; Murtola, T.; Schulz, R.; Páll, S.; Smith, J.; Hess, B.; Lindahl, E. GROMACS: High performance molecular simulations through multi-level parallelism from laptops to supercomputers. *SoftwareX* **2015**, *1–2*, 19–25.

(31) Sorichetti, V.; Hugouvieux, V.; Kob, W. Determining the mesh size of polymer solutions via the pore size distribution. *Macromolecules* **2020**, *53*, 2568–2581.

(32) Rubinstein, M.; Colby, R. H. *Polymer Physics*; Oxford University Press: Oxford, New York, 2003.

(33) Chen, R.; Poling-Skutvik, R.; P. Howard, M.; Nikoubashman, A.; A. Egorov, S.; C. Conrad, J.; C. Palmer, J. Influence of polymer flexibility on nanoparticle dynamics in semidilute solutions. *Soft Matter* **2019**, *15*, 1260–1268.

(34) Yasuda, H.; Lamaze, C. E.; Peterlin, A. Diffusive and hydraulic permeabilities of water in water-swollen polymer membranes. *J. Polym. Sci. Part A-2: Polym. Phys.* **1971**, *9*, 1117–1131.

(35) Cohen, M. H.; Turnbull, D. Molecular transport in liquids and glasses. *J. Chem. Phys.* **1959**, *31*, 1164–1169.

TOC Graphic

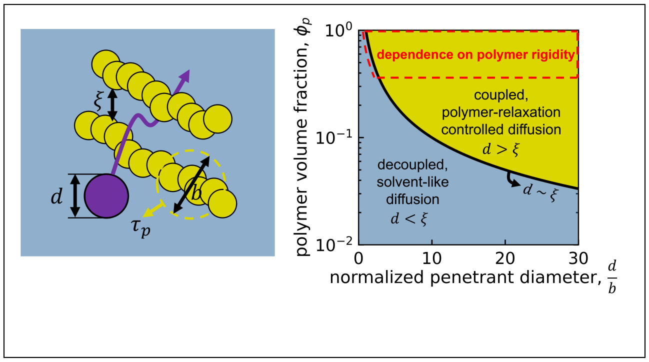
ξ
d
b
τ_p
polymer volume fraction, ϕ_p
10^0
10^-1
10^-2
0
10
20
30
normalized penetrant diameter, d/b
dependence on polymer rigidity
coupled,
polymer-relaxation
controlled diffusion
d > ξ
decoupled,
solvent-like
diffusion
d < ξ
d ~ ξ

Supporting Information: Influence of Rigidity-Hydration Coupling on Size-Dependent Diffusion in Hydrated Polymer Membranes

Paul R. Irving, Soham Rane, Benny D. Freeman,* and Venkat Ganesan*

Department of Chemical Engineering, University of Texas at Austin

E-mail: freeman@che.utexas.edu; venkat@che.utexas.edu

Simulation Details

Coarse-grained molecular dynamics (CGMD) simulations were performed using the GROMACS 2020.5 software package.[1–8] Monomer, solvent, and penetrant beads interacted via the Lennard-Jones (LJ) potential:[9]

$$U_{\mathrm{ij}}(r) = 4\epsilon_{\mathrm{ij}}\left[\left(\frac{\sigma_{\mathrm{ij}}}{r}\right)^{12} - \left(\frac{\sigma_{\mathrm{ij}}}{r}\right)^{6}\right] \tag{S1}$$

where U_{ij} is the potential energy between particles i and j, r is their separation, ϵ_{ij} is the interaction well depth, and σ_{ij} is the zero-energy separation distance. A cutoff distance of 3.0σ with the potential shifted to zero at the cutoff was used. All beads were assigned $\epsilon_{\mathrm{ii}} = \epsilon_{\mathrm{ij}} = 1\epsilon$ and mass $m_i = 1m$. For solvent and monomer beads, $\sigma_{\mathrm{ii}} = 1\sigma$, while the penetrant bead size σ_{ii} was varied from 0.25σ to 2.0σ. Mixed interaction lengths were computed using the arithmetic mixing rule:[9]

$$\sigma_{\mathrm{ij}} = \frac{1}{2}\left(\sigma_{\mathrm{ii}} + \sigma_{\mathrm{jj}}\right) \tag{S2}$$

All quantities were reported in reduced LJ units, which can be converted to real units by specifying σ, ϵ, and m.

While penetrant species are modeled with identical Lennard–Jones interaction strengths, varying their diameter introduces subtle thermodynamic differences. In bulk fluids, smaller particles exhibit a higher cohesive energy density due to their larger number density, and mixtures of different-sized particles can display enhanced packing efficiency. However, in the present simulations, penetrants are at dilute concentrations and do not significantly perturb the polymer matrix (as evidenced by the insensitivity of pore size distributions to penetrant size in Figure S2B), so size-dependent transport primarily reflects differences in excluded volume and accessibility of the existing free-volume landscape.

Linear polymer chains were constructed from 50 monomer beads connected by finitely extensible nonlinear elastic (FENE) bonds:

$$U_{\mathrm{FENE}} = -\frac{k_b R_0^2}{2} \log\left(1 - \frac{r^2}{R_0^2}\right) \tag{S3}$$

where $k_b = 70\epsilon/\sigma^2$ is the bond stiffness and $R_0 = 1.5\sigma$ is the maximum bond length. Polymer rigidity was modulated via harmonic bond angle interactions:[9–13]

$$U_\theta = \frac{k_\theta}{2}(\theta - \theta_0)^2 \tag{S4}$$

where θ is the angle formed by three consecutive monomer beads, θ_0 is the equilibrium angle (set equal to 114°, analogous to a polyethylene chain[14]), and k_θ is the angular force constant which was varied to modulate chain flexibility.

Simulation boxes of length 23σ contained a total of 10,000 monomer and solvent beads, along with 20 penetrant beads. The system temperature was maintained at 0.75ϵ,[15,16] and the integration time step was $0.05\sigma\sqrt{m/\epsilon}$. Temperature control was implemented via a velocity rescaling thermostat with relaxation time $\tau_T = 1.0\sigma\sqrt{m/\epsilon}$. An equilibration protocol (Table S1) was followed prior to production runs.[16,17] During production, energy traces were monitored to ensure equilibration, and all analyses were conducted after energies stabilized. Production run simulation times varied from $40,000\tau$ to $90,000\tau$ with longer run-times corresponding to simulations with either slow equilibration or slow system dynamics (i.e. systems with low water content or high chain rigidity).

Table S1: Equilibration procedure for CGMD simulations.[15,17] $P^* = \epsilon/\sigma^3$, $\tau = \sigma\sqrt{m/\epsilon}$

Step	Conditions	Number of timesteps
1	Energy minimization	steepest descent
2	NVT	10,000
3	NPT, $P = 0.727P^*$, $\tau_p = 0.5\tau$	50,000
4	NPT, $P = 0.727P^*$, $\tau_p = 1.0\tau$	100,000
5	NVT	100,000

Penetrant diffusivity was extracted from mean square displacement (MSD) calculations:

$$\lim_{t\to\infty} \langle |\mathbf{r}(t) - \mathbf{r}(0)|^2 \rangle = 6Dt \tag{S5}$$

where D is the diffusion coefficient, and $\mathbf{r}(t)$ and $\mathbf{r}(0)$ are the penetrant positions at time, t, and $t = 0$, respectively. The time range for computing the diffusivity during the production run varied depending on rigidity, penetrant size, and water content. Typically, longer times were required to reach the diffusive regime for slower systems (high rigidity, low water content, large penetrant size). We restricted diffusivity fitting to the regime where log(MSD) vs. log(t) had a slope of 1.0 (i.e., from 0.8 to 1.2) to ensure penetrant motion was diffusive rather than sub-diffusive/ballistic. In simulations where the diffusive regime was not reached, diffusivity values are omitted in the dataset.

The dynamic structure factor was computed as:[18]

$$S(q,t) = \frac{1}{N^2} \sum_{i,j} \exp\left[i\mathbf{q} \cdot (\mathbf{r}_i(t) - \mathbf{r}_j(0))\right] \tag{S6}$$

where $\mathbf{q}$ is the wavevector of magnitude, q, chosen as $\mathbf{q} = \frac{2\pi}{L}\langle n_x, n_y, n_z\rangle$, for box length, L, and n_i are integer components. The decay of $S(q,t)$ was fit to a stretched exponential:[18,19]

$$\frac{S(q,t)}{S(q,0)} = \exp\left[-\left(\frac{t}{a}\right)^{b}\right] \tag{S7}$$

where a and b are fitting parameters. The corresponding polymer structural relaxation time τ_p was obtained as:[18,19]

$$\tau_p = a\Gamma\left(1+\frac{1}{b}\right) \tag{S8}$$

where Γ is the gamma function. The τ_p values plotted in Figure 2B correspond to τ_p values at a characteristic size, $2\pi/q$, of 1.0σ. Plots of τ_p vs. $2\pi/q$ are presented in Figure S3.

Pore size distributions (PSDs) were computed using the PoreBlazer v4.0 software. For PSD calculations, penetrant and solvent beads were removed from the simulation box, and polymer beads were assigned a diameter of 1σ. The minimum probe size 0.2σ was chosen to be smaller than the minimum penetrant diameter (0.25σ), allowing assessment of accessible volume for all penetrant sizes. Polymer correlation length was computed from the PSD according to Sorichetti *et al.*:[20]

$$\xi = \int_0^\infty xPSD(x)dx \tag{S9}$$

where x is the pore diameter and $PSD(x)$ is the normalized pore size distribution.

For the fully solvated system ($\phi_w = 1.0$), solvent beads were retained during the PSD calculation. The average free-volume element diameter was computed analogously as:

$$\langle d_p\rangle = \int_0^\infty xPSD(x)dx \tag{S10}$$

and the corresponding average free-volume element size was calculated as $\pi\langle d_p\rangle^3/6$.

Polymer Kuhn lengths were computed using:

$$b = \frac{\langle R^2\rangle}{R_{\max}} \tag{S11}$$

where $\langle R^2 \rangle$ is the mean-square end-to-end distance of the polymer in a melt or in θ-solvent and $R_{\max}$ is the fully extended chain length:

$$R_{\max} = nl \sin\left(\frac{\theta}{2}\right) \tag{S12}$$

where n is the number of bonds along the polymer backbone, l is the average bond length, and θ is the backbone bond angle. Since our simulations approximate those of a θ-solvent ($\epsilon_{\text{polymer}-\text{polymer}} = \epsilon_{\text{solvent}-\text{solvent}} = \epsilon_{\text{polymer}-\text{solvent}}$), we calculated Kuhn length from simulations at $\phi_w = 0.79$.

Diffusivity Models

Stokes-Einstein

Comparison of the Stokes-Einstein model (Equation 2 in the main text) with simulation data is provided in Figure S1. Figure S1A includes data for polymer-free systems (solvent and penetrant only). As shown, diffusivity follows Stokes-Einstein with a slope of -1.10. However, as shown in Figure S1B, systems with a water volume fraction of 0.29 show significant deviation from Stokes-Einstein with slopes ranging from -1.62 to -3.12 in moving from flexible to rigid polymers.

Polymer Physics Models

Theoretical models for penetrant diffusion in polymer solutions depend on the correlation length, ξ, which provides a measure of the spacing between polymer segments. While calculating a single value of ξ is useful, there is always a distribution of chain spacings, which can be quantified from simulations via pore size distributions (PSDs), as shown in Figure S2.

PSDs for simulations with varying ϕ_w and k_θ are shown in Figure S2A (for penetrants with diameter of 1.75σ) and PSDs with varying ϕ_w and penetrant diameter are shown in Figure

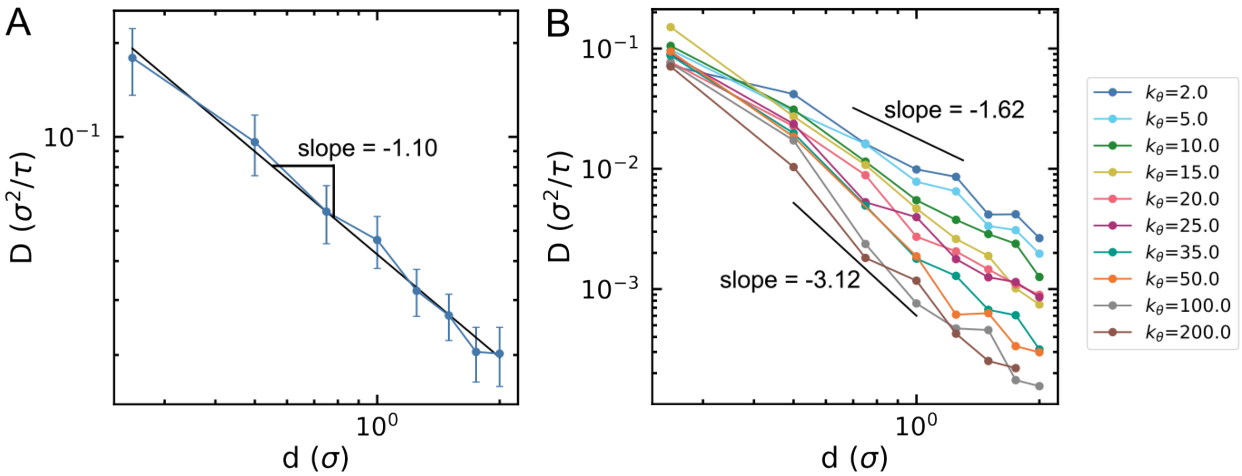

Figure S1: CGMD simulation results for (A) diffusivity of penetrant beads vs. penetrant diameter in solvent (i.e. polymer free, $\phi_w \approx 1.0$). Diffusivity follows the Stokes-Einstein equation, with a slope of -1.10. (B) Diffusivity of penetrant beads vs. penetrant diameter in a polymer solution ($\phi_w = 0.29$). Diffusivity deviates from the Stokes-Einstein relationship. The presence of polymer with higher rigidity causes a more pronounced deviation from Stokes-Einstein, with diffusivity showing a stronger dependence on diameter. Reduced Lennard-Jones (LJ) units are used for diffusivity and diameter values, where σ is the LJ diameter and $\tau = \sigma\sqrt{m/\epsilon}$, where m is the bead mass and ϵ is the LJ well depth.

S2B (for simulations with $k_\theta = 200.0\epsilon/\text{rad}^2$). As shown, computed PSDs show a strong dependence on solvent content, but negligible dependence on polymer backbone rigidity or penetrant diameter. Correlation length can be computed from pore-size distributions using Equation S9. In Figure S2C, we plot the correlation length vs. the polymer volume fraction, where we have averaged over every rigidity value and penetrant diameter value. As shown, a plot of $\log \xi$ vs. $\log \phi_p$ has a slope of -1.15. Theoretically, $\xi \sim \phi_p^{-\nu/(3\nu-1)}$, where ν is the Flory exponent, equal to 0.5 in θ-solvent and 0.588 in good solvent. Therefore, in θ-solvent one expects a slope of -1 and in good solvent one expects a slope of -0.77. Our simulations approximate that of a θ-solvent due to polymer-polymer, solvent-solvent, and polymer-solvent interactions all having equal energy. Therefore, the computed slope of -1.15 is approximately consistent with theory. The computed values for ξ range from 0.79σ to 3.27σ for nominal water volume fractions ranging from 0.17 to 0.75. Since penetrant diameter ranges from 0.25σ to 2σ, we are exploring regimes where $d < \xi$ and $d > \xi$.

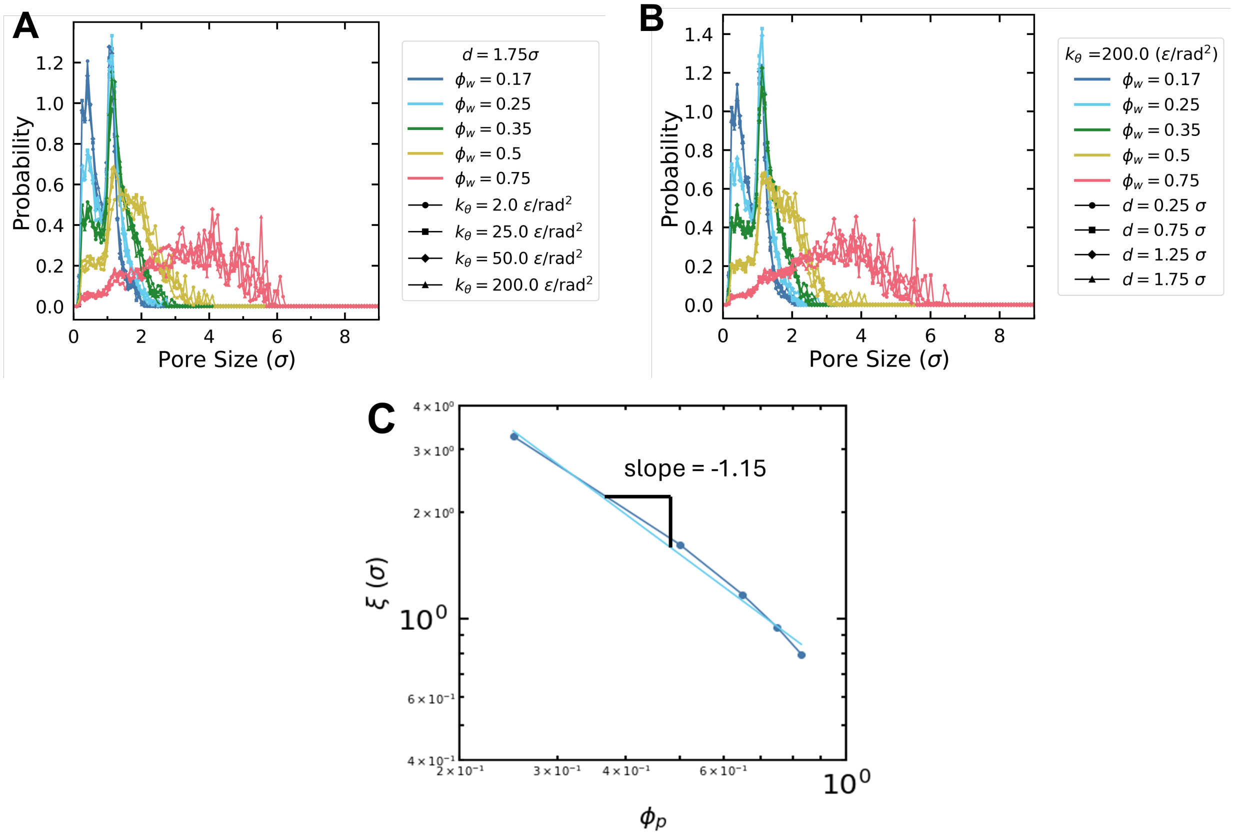

Figure S2: Pore size distributions for (A) simulations with $d = 1.75\sigma$ with varying solvent content and backbone rigidity and (B) simulations with $k_\theta = 200.0\epsilon/\mathrm{rad}^2$ and varying solvent content and bead diameter. As shown, the PSD's show a strong dependence on water content, but a weak dependence on the backbone dynamics and the size of the penetrant bead present. (C) Correlation length vs. polymer volume fraction. The plot shows a slope of -1.15, approximately matching the expected scaling of -1 in θ-solvent.

The coupling and decoupling of penetrant diffusivities from polymer dynamics is critical for tuning membrane separation performance. Large penetrants are often trapped by polymer segments more than small penetrants, and therefore show a stronger coupling to polymer dynamics. By increasing rigidity, the diffusion of large penetrants decreases significantly while small penetrants are less affected. Therefore, increasing rigidity can cause an increase in selectivity while maintaining diffusivity of the faster species, resulting in an improvement of separation performance.

The dependence of polymer dynamics on length-scale is well-studied in the polymer physics community:[21]

$$\tau_p \approx \begin{cases} \tau_0 \left(\frac{d}{b}\right)^3 & , d < \xi \text{ (Zimm)} \\ \tau_\xi \left(\frac{d}{\xi}\right)^4 & , d > \xi \text{ (Rouse)} \end{cases} \tag{S13}$$

where b is the Kuhn length, d is the length-scale of interest, and τ_0 is given as:

$$\tau_0 \approx \frac{\eta_s b^3}{k_B T} \tag{S14}$$

and τ_ξ is given as:

$$\tau_\xi \approx \frac{\eta_s \xi^3}{k_B T} \tag{S15}$$

where η_s is the solvent viscosity.

As shown in Figure S3A, at a high water volume fraction of 0.79, the simulated polymer relaxation, computed from the decay of the dynamic structure factor (Equations S6-S8), appears to follow the scaling with d^3 predicted from the Zimm model. As shown in Figure S3B, at a lower water volume fraction of 0.20, the agreement with theory is not as accurate. As described in the main text, τ_p shows a very strong dependence on polymer rigidity, which is expected when $\xi \sim b$, but not directly incorporated into Equations S13-S15. As will be described later, free volume models can be used to describe relaxation of Kuhn segments rather than using Stokes-Einstein with solvent viscosity as is done in Equations S13-S15.

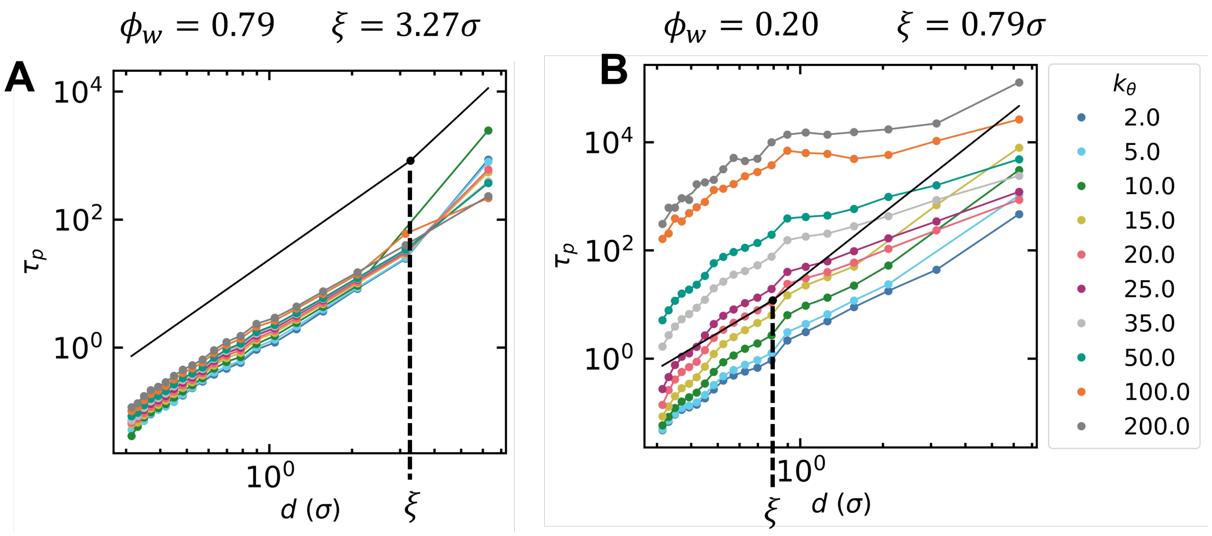

Figure S3: Polymer relaxation times, τ_p, computed using Equations S6-S8 vs. characteristic spacing $d = 2\pi/q$. (A) Plot at a water volume fraction of 0.79, (B) plot at a water volume fraction of 0.20. The slopes of the solid black lines represent the predicted scaling from Equation S13, which transitions from a slope of 3 to a slope of 4 at $d = \xi$.

Free Volume Models

Free-volume models typically assume the following dependence of penetrant diffusivity on size and free volume:[22]

$$D = A \exp\left(-\frac{V^*}{V_f}\right) \tag{S16}$$

where A is a pre-exponential factor, V^* is a parameter with strong dependence on penetrant size (often assumed to be proportional to the penetrant cross-sectional area times the diffusion jump distance), and V_f is the effective average free volume element size that has been corrected to account for the overlap free volume.

Yasuda Model

Based on the free-volume concept, Yasuda *et al.* derived the following expression for penetrant diffusivity in hydrated polymer systems:[23]

$$D = D_w \exp\left(\frac{\beta\left(\alpha - 1\right)\left(1 - \phi_w\right)}{\phi_w + \alpha\left(1 - \phi_w\right)}\right) \tag{S17}$$

where ϕ_w is the water volume fraction, α and β are given as:

$$\alpha = V_{f,p}/V_{f,w} \tag{S18}$$

$$\beta = V^*/V_{f,w} \tag{S19}$$

where $V_{f,p}$ is the polymer fractional free volume, and $V_{f,w}$ is the water fractional free volume. As such, α is a polymer-specific parameter. Approximating V^* as the penetrant volume, β is a penetrant-specific parameter, and Equation S17 predicts a linear scaling of $\log D$ with d^3. As shown in Figure S4, scaling of $\log D$ with d^3 (at a water volume fraction of 0.29) does not agree well with our simulation data as compared to scaling of $\log D$ with $\log d$ in Figure S1B.

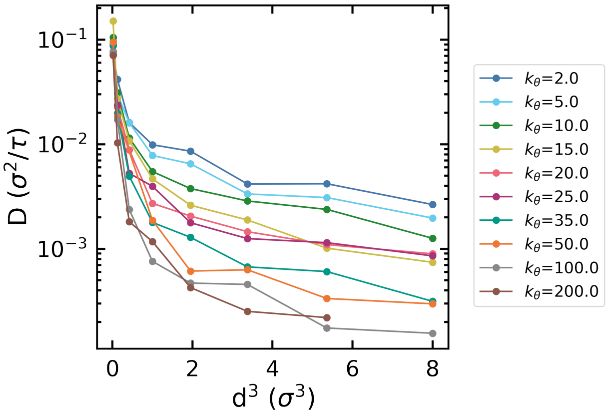

Figure S4: Plot of diffusivity vs. d^3 in a polymer solution ($\phi_w = 0.29$). The plot shows significant nonlinearity, suggesting a deviation from the Yasuda model provided in Equations S17-S19. Comparison with Figure S1B suggests that the scaling of $\log D$ with $\log d$ is superior.

Beyond the predicted scaling, the parameters in the Yasuda model can be computed directly from simulations. α can be computed as $\mathrm{FFV}_p/\mathrm{FFV}_w$ where FFV is the fractional free-volume. For this calculation, we assume that polymer and solvent beads have a diameter of 1σ and use the simulation box volumes for polymer-free and solvent-free cases to obtain FFV_w and FFV_p, respectively. This approach yielded an FFV_w value of 0.57 from polymer-free systems. FFV values for pure polymer were calculated for each polymer backbone rigidity and are provided in Table S2. They ranged from 0.46 for $k_\theta = 2.0\epsilon/\mathrm{rad}^2$ to 0.51 for $k_\theta = 200.0\epsilon/\mathrm{rad}^2$.

Table S2: Dependence of polymer fractional free volume ($\mathrm{FFV_p}$) on backbone rigidity, k_θ

k_θ (ϵ/rad^2)	FFV_p
2.0	0.46
5.0	0.46
10.0	0.46
15.0	0.46
20.0	0.46
25.0	0.46
35.0	0.47
50.0	0.47
100.0	0.49
200.0	0.51

We attribute the larger free volume of the rigid polymer systems to the nonequilibrium excess volume of a glassy material. α therefore ranges from 0.81 for $k_\theta = 2.0\epsilon/\mathrm{rad}^2$ to 0.90 for $k_\theta = 200.0\epsilon/\mathrm{rad}^2$. These values are consistent with experimental positron annihilation lifetime spectroscopy (PALS) measurements and atomistic simulations of PEO-based polymers which have suggested α should range from 0.75 to 1.0.[18] β can be computed by assuming V^* is the penetrant volume and $V_{f,w} = \pi\langle d_p\rangle^3/6$, with $\langle d_p\rangle$ computed from solvent-only PSDs (Equation S10). Using this approach, we compute an average free volume element diameter of 0.49σ corresponding to an average free volume element size of $0.06233\sigma^3$. Prediction of penetrant diffusivity using computed values for α and β leads to very poor agreement with simulation data. In addition to poor numerical agreement, the model incorrectly predicts the dependence of diffusivity on polymer rigidity. The positive correlation between k_θ and α implies that an increase in polymer rigidity will correspond to an increase in penetrant diffusivity based on Equation S17. Based on our simulations, this trend is incorrect. Instead, it is expected that α should decrease as k_θ increases. This observation suggests that a static view of free volume is insufficient for correlation with dynamic properties such as diffusivity when polymer chemistry and polymer dynamics are changed. This observation is perhaps not surprising, since many glassy materials have large nonequilibrium free volume as compared to rubbery materials but also have lower penetrant diffusion coefficients.

Alternatively, α and β can be treated as fitting parameters. One way to fit the data is to fit $\log(D)$ vs. ϕ_w data for each unique k_θ value and penetrant diameter. Therefore, α and β are both allowed to vary with penetrant size and backbone flexibility, while D_w is fixed at the measured diffusivity in the polymer-free simulation. However, such a fitting procedure leads to significant overfitting, and leads to α and β values that appear to have a random dependence on backbone flexibility and size. Alternatively, one can allow β to vary only with penetrant size (i.e. independent of backbone flexibility) and allow α to vary only with backbone flexibility (i.e. independent of penetrant size). The polymer-free diffusivity, D_w, can be computed from Stokes-Einstein (Equation 2), where $k_BT/(3\pi\eta_s)$ represents a single fitting parameter. In Figure S5A, we compare modeled diffusivities with simulated diffusivities in a parity plot. As shown, the model provides a good fit to the data, with an R^2 of 0.982.

Computed values for α and β are plotted in Figure S5B and C, respectively. As shown, α monotonically decreases with increasing rigidity (k_θ), and β monotonically increases with increasing penetrant diameter (d). Therefore, although α and β are fitting parameters, they maintain some level of physical significance.

Modified Diffusivity Model

While the Yasuda model provides a good fit to the simulation data, the model is limited by the unknown dependence of β on penetrant size. Here, we derive a modified version of the model which has an explicit dependence on penetrant diameter, rather than β, and incorporates the observation that a sufficiently small penetrant, with diameter, d_0, will have constant diffusivity, D_0, regardless of water volume fraction or polymer rigidity. This idea is shown in Figure S6, where the diffusivity of penetrants with a diameter of 0.25σ shows minimal dependence on either water volume fraction or polymer rigidity.

If one assumes a linear relationship between $\log D$ and $\log d$, the following relationship

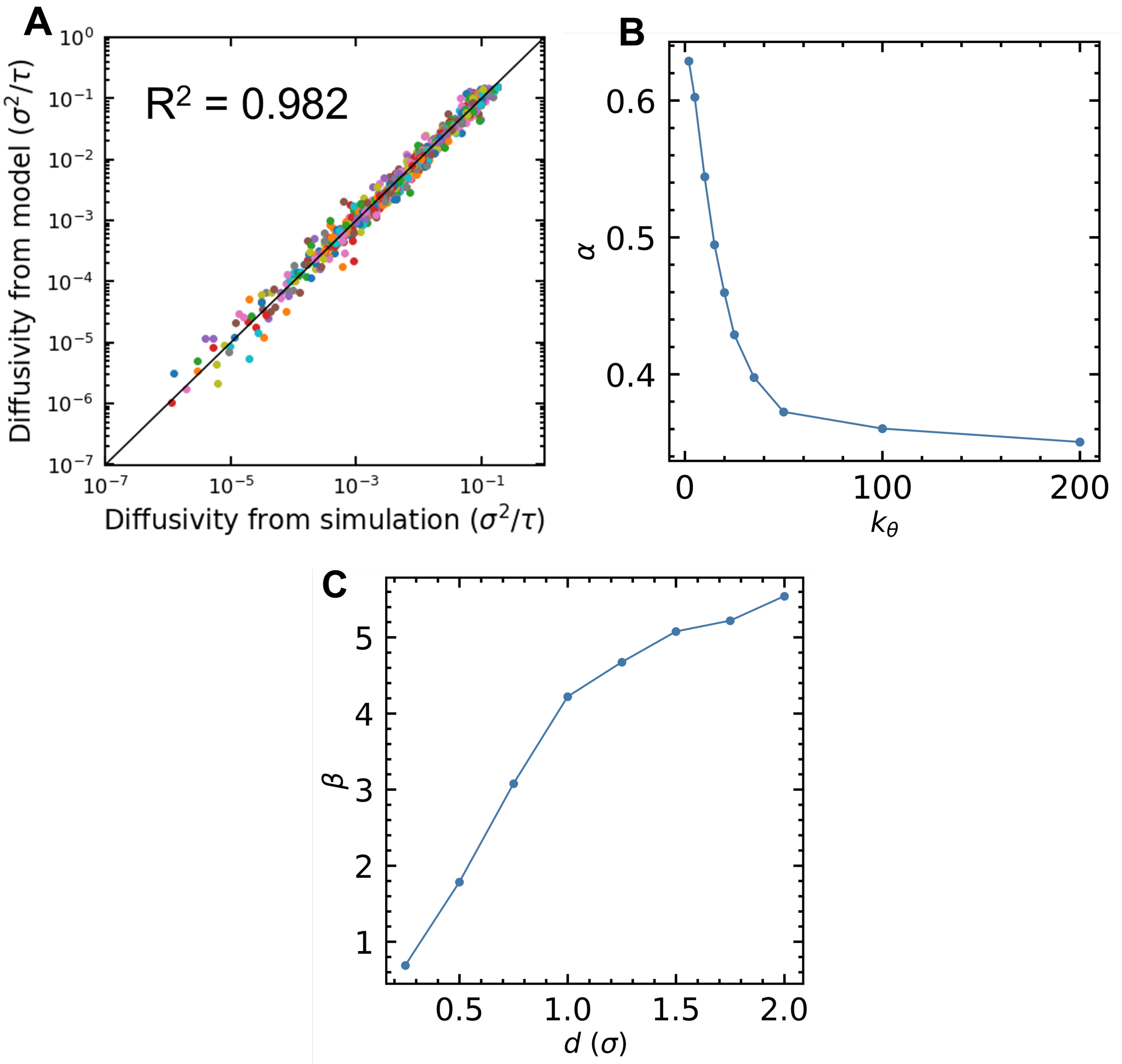

Figure S5: Plots of (A) modeled vs. simulated diffusivity plotted on a parity plot, (B) α vs. k_θ and (C) β vs. d, obtained from fitting simulation data to the Yasuda model (Equation S17).

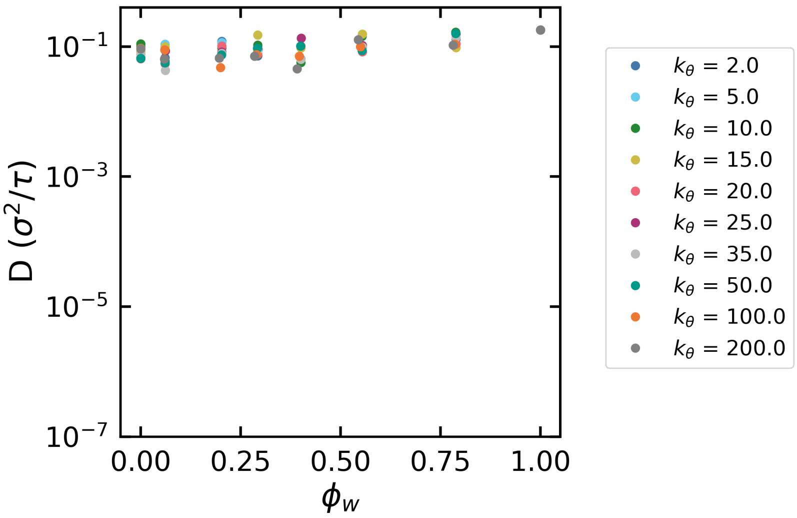

Figure S6: Diffusivity vs. water volume fraction for penetrants with $d = 0.25\sigma$. As shown, diffusivity shows minimal dependence on either water volume fraction or polymer rigidity, indicative of a decoupling from polymer and water dynamics.

will be obeyed:

$$\frac{D}{D_0} = \left(\frac{d_0}{d}\right)^{\gamma} \tag{S20}$$

where γ is the scaling exponent. Setting the diffusivity, D, from this model equal to that of the Yasuda model, and letting $D_w = D_0 d_0/d$ (Stokes-Einstein), one obtains:

$$(\gamma - 1)\ln\left(\frac{d_0}{d}\right) = \frac{\beta(\alpha - 1)(1 - \phi_w)}{\phi_w + \alpha(1 - \phi_w)} \tag{S21}$$

Here, γ is a function only of rigidity (α) and water content (ϕ_w), while β is a function of penetrant size. Equation S21 suggests that β can be redefined to be proportional to $\ln(d/d_0)$ rather than proportional to d^3 as suggested in the original Yasuda model. This proportionality recovers a scaling between $\log D$ and $\log d$ which is in better agreement with our simulation data than between $\log D$ and d^3, as shown by comparing Figures S4 and S1B. Therefore, if we let $\beta = (B + 1)\ln(d/d_0)$, with $B + 1$ defined as a proportionality constant capturing the strength of size-dependence, then:

$$\gamma = 1 - \frac{(B + 1)(\alpha - 1)(1 - \phi_w)}{\phi_w + \alpha(1 - \phi_w)} = \frac{1 + B(1 - \phi_w)(1 - \alpha)}{\phi_w + \alpha(1 - \phi_w)} \tag{S22}$$

Therefore, the final form of the model is:

$$D = D_0 \left(\frac{d_0}{d}\right)^{\frac{1+B(1-\phi_w)(1-\alpha)}{\phi_w+\alpha(1-\phi_w)}} \tag{S23}$$

Fits to Equation S23 to the simulation data are provided in Figure S7. As shown, the model properly captures the quantitative simulated trends. A parity plot of the simulated and modeled data is provided in Figure 3 in the main text.

Plots of Kuhn length vs. k_θ, α vs. k_θ, and α vs. Kuhn length are provided in Figure S8. As polymer rigidity increases (i.e. k_θ increases), the Kuhn length increases and α decreases. $\log \alpha$ vs. Kuhn length is approximately linear, allowing the number of fitting parameters to be reduced from 13 to 5, with minimal change to the fit, as shown in Figure S9.

The relaxation of Kuhn segments can be expected to obey a similar mechanism as the diffusion of penetrant beads, as governed by free volume. This tendency is the main source of discrepancy between theories for nanoparticle diffusion and our simulation results. The Cai model assumes that Kuhn segment relaxation times are predicted directly from Stokes-Einstein with the solvent viscosity. Indeed, as shown in Figure 2B, the inverse of polymer relaxation time shows similar dependence on water content as diffusion of penetrants.

A polymer segment diffusivity can be computed from the modified diffusion model:

$$D_{p0} = D_0 \left(\frac{d_0}{b}\right)^{\frac{1+B(1-\phi_w)(1-\alpha)}{\phi_w+\alpha(1-\phi_w)}} \tag{S24}$$

The relaxation timescale is then given as:

$$\tau_{p0} = \frac{b^2}{D_{p0}} \tag{S25}$$

As shown in Figure S10, the computed τ_{p0} values from the model correlate with the τ_{p0} values from simulation, which were calculated as the value of τ_p at $q = 2\pi/b$.

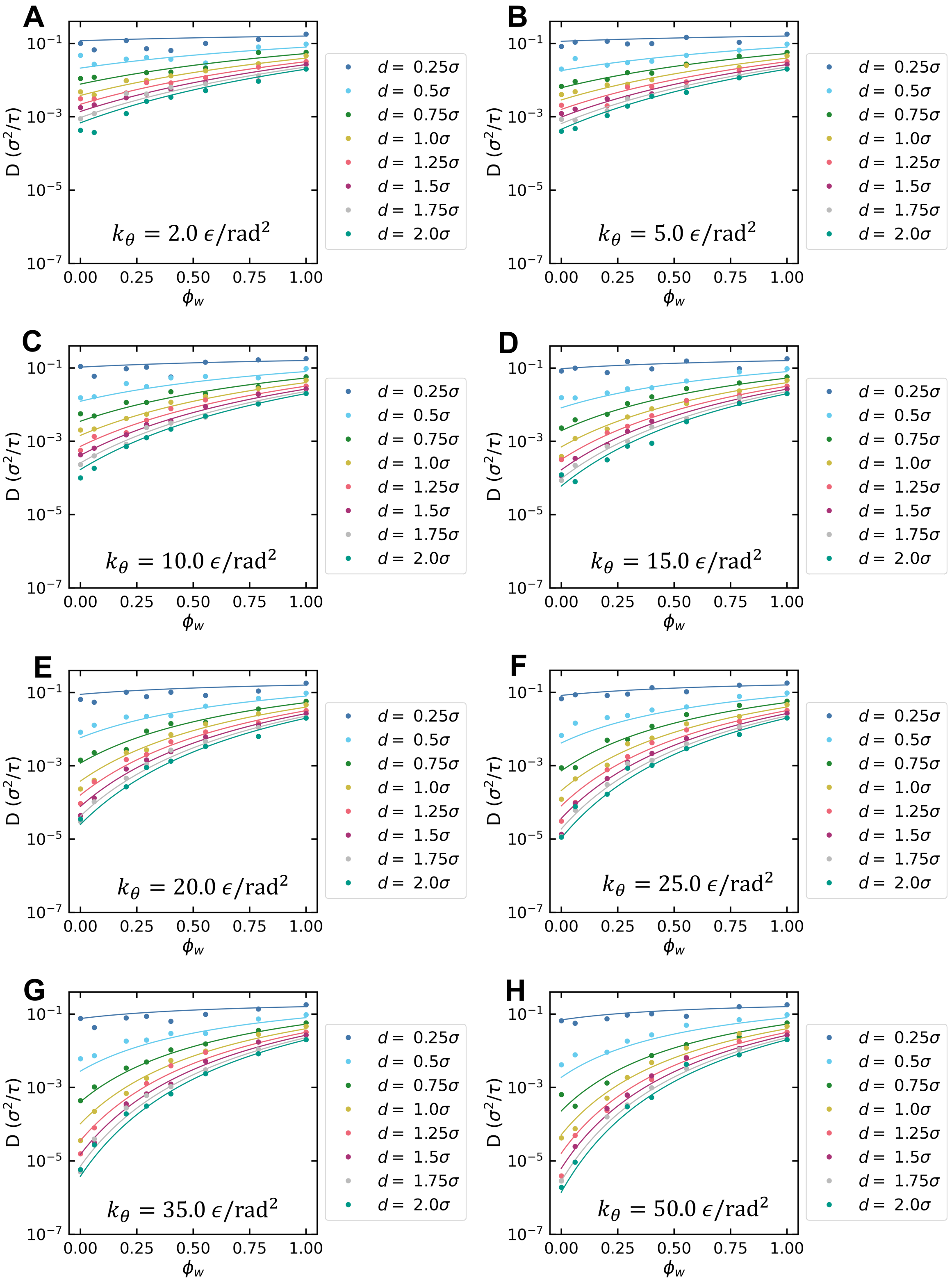
A
B
C
D
E
F
G
H
D (σ^2/τ)
10^{-1}
10^{-3}
10^{-5}
10^{-7}
0.00
0.25
0.50
0.75
1.00
ϕ_w
$k_\theta = 2.0\ \epsilon/\mathrm{rad}^2$
$k_\theta = 5.0\ \epsilon/\mathrm{rad}^2$
$k_\theta = 10.0\ \epsilon/\mathrm{rad}^2$
$k_\theta = 15.0\ \epsilon/\mathrm{rad}^2$
$k_\theta = 20.0\ \epsilon/\mathrm{rad}^2$
$k_\theta = 25.0\ \epsilon/\mathrm{rad}^2$
$k_\theta = 35.0\ \epsilon/\mathrm{rad}^2$
$k_\theta = 50.0\ \epsilon/\mathrm{rad}^2$
$d =$ 0.25σ
$d =$ 0.5σ
$d =$ 0.75σ
$d =$ 1.0σ
$d =$ 1.25σ
$d =$ 1.5σ
$d =$ 1.75σ
$d =$ 2.0σ

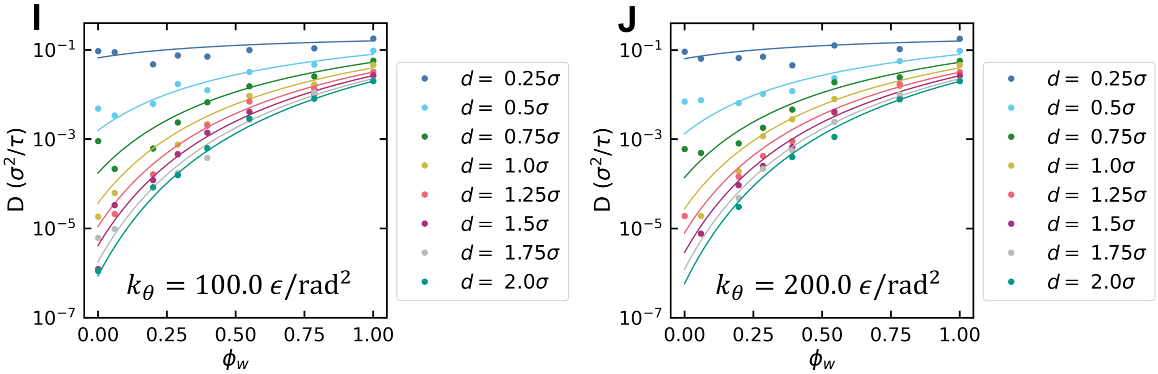

Figure S7: Plots of penetrant diffusivity vs. water volume fraction for varying penetrant diameter. Lines are fits to Equation S23. The following parameters were used for the fits: $D_0 = 0.1944\sigma^2/\tau$, $d_0 = 0.2049\sigma$, $B = 1.563$. (A) $\alpha = 0.6339$ ($k_\theta = 2.0\epsilon/\text{rad}^2$) (B) $\alpha = 0.6073$ ($k_\theta = 5.0\epsilon/\text{rad}^2$) (C) $\alpha = 0.5504$ ($k_\theta = 10.0\epsilon/\text{rad}^2$) (D) $\alpha = 0.5015$ ($k_\theta = 15.0\epsilon/\text{rad}^2$) (E) $\alpha = 0.4663$ ($k_\theta = 20.0\epsilon/\text{rad}^2$) (F) $\alpha = 0.4364$ ($k_\theta = 25.0\epsilon/\text{rad}^2$) (G) $\alpha = 0.4053$ ($k_\theta = 35.0\epsilon/\text{rad}^2$) (H) $\alpha = 0.3792$ ($k_\theta = 50.0\epsilon/\text{rad}^2$) (I) $\alpha = 0.3677$ ($k_\theta = 100.0\epsilon/\text{rad}^2$) (J) $\alpha = 0.3584$ ($k_\theta = 200.0\epsilon/\text{rad}^2$).

Mackie-Meares Model

Another common model for penetrant diffusivity is the Mackie-Meares model:

$$D = D_w \left(\frac{\phi_w}{2 - \phi_w} \right)^2 \tag{S26}$$

This model allows diffusivity to be estimated with no fitting parameters. The model assumes the polymer is completely immobile and that polymer beads, solvent beads, and penetrant beads all occupy a single point on a lattice, and are therefore approximately the same size. Based on these assumptions, we may expect the model to work reasonably well for our simulations with rigid polymers and a penetrant diameter of $d = 1\sigma$. As shown in Figure S11, the model does indeed provide a good fit, where the yellow points represent the simulated diffusivity values and the dashed line is a plot of Equation S26. The model also provides an excellent prediction for diffusivity of penetrants with $d = 0.75\sigma$. However, the model prediction is much worse for the other penetrant bead sizes. One explanation for this discrepancy is that for larger (smaller) penetrant beads, the accessible volume fraction is

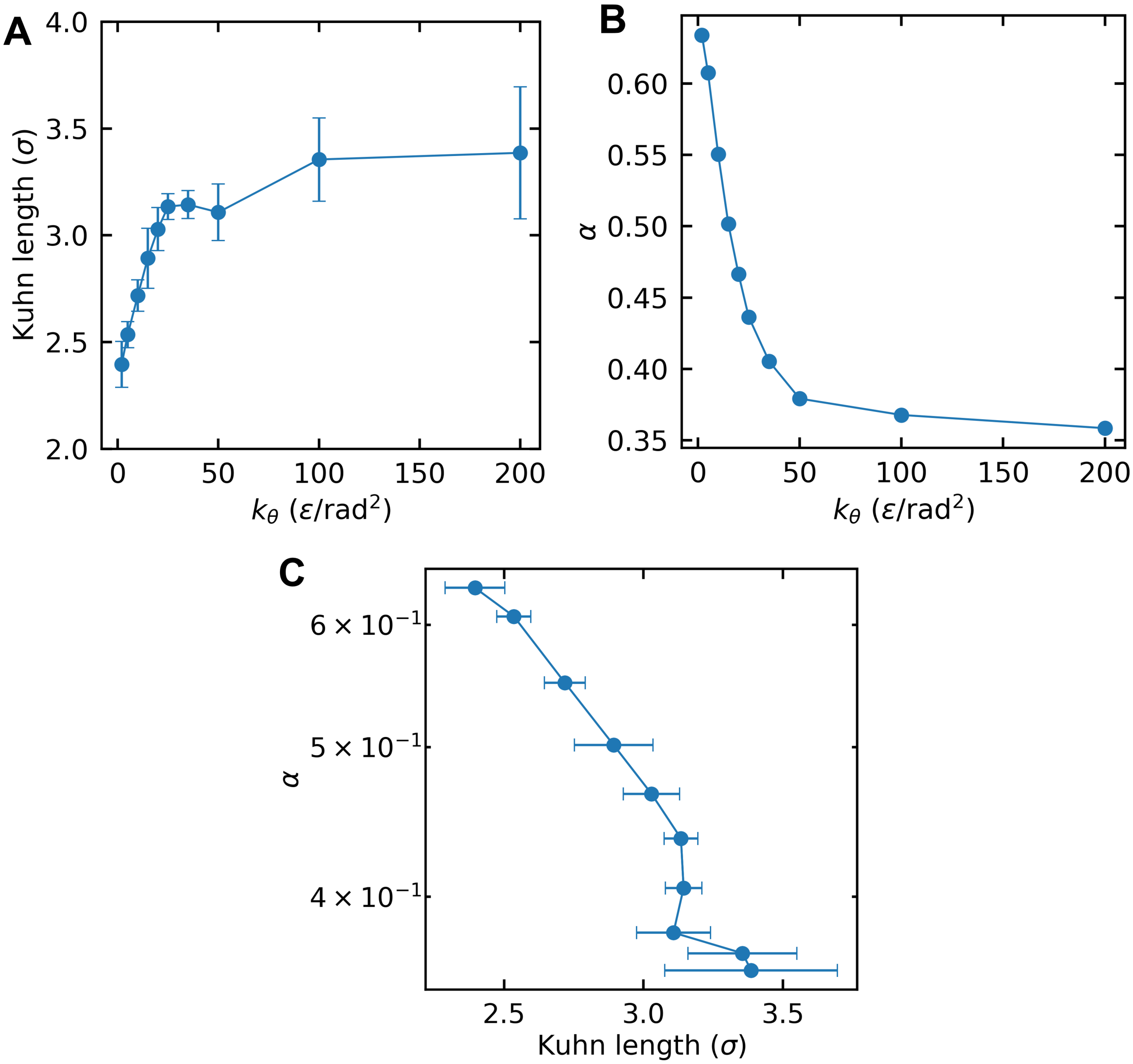

Figure S8: (A) Kuhn length vs. k_θ, (B) α vs. k_θ, (C) α vs. Kuhn length.

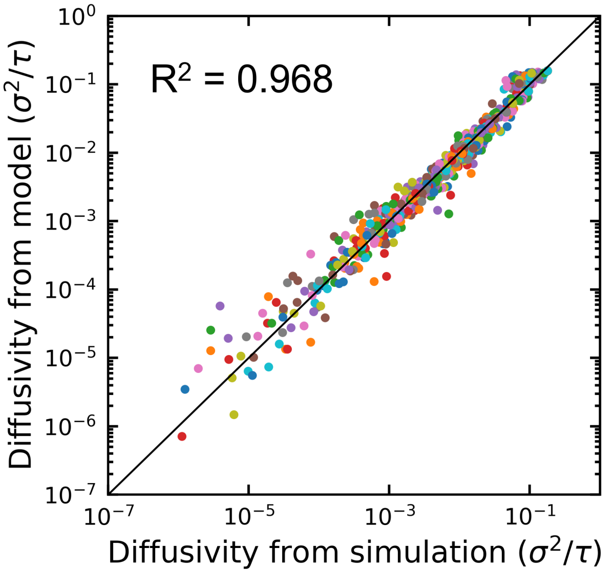

Figure S9: Parity plot for modified Yasuda model with simplified relationship between α and Kuhn length.

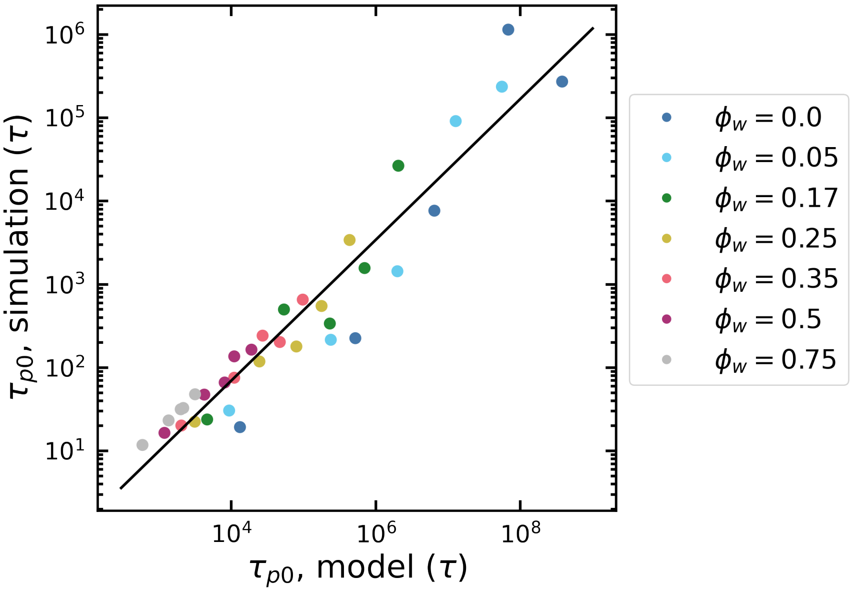

Figure S10: Comparison of model prediction for polymer relaxation dynamics with simulated quantities.

smaller (larger) than for a penetrant with size equal to the lattice size (i.e., size equal to the solvent and polymer bead sizes). To account for this difference in accessible volume, we can modify Equation S26:

$$D = D_w \left(\frac{f\phi_w}{2 - f\phi_w} \right)^2 \tag{S27}$$

where f represents the fraction of the water volume fraction accessible to the penetrant, computed as:

$$f = \frac{\int_d^\infty PSD(x)\,dx}{\int_{1\sigma}^\infty PSD(x)\,dx} \tag{S28}$$

For penetrants larger than the lattice size, $f < 1$, and for penetrants smaller than the lattice size, $f > 1$. Equations S27 and S28 can be used to estimate diffusivities with no fitting parameters by using the computed PSD's. However, for larger bead sizes, this procedure tended to under-predict the simulated diffusivity values. If we instead treat d in Equation S28 as a fitting parameter, then we obtain good agreement, as plotted in Figure S11. The values for d fitted by the model differ from the actual values. For example, for $d = 0.25$, the fitted value of d is equal to 0.0σ, indicating that the entire PSD is integrated. For $d = 2.0$, we compute a fitted value of 1.36σ. Additionally, this form of the model assumes the polymer is completely immobile and therefore does not predict any dependence of diffusivity on polymer dynamics. As a result, we are only able to make a reasonable comparison with data for the most rigid polymers ($k_\theta = 200.0\epsilon/\mathrm{rad}^2$). Due to these shortcomings, we believe the model is not as useful for modeling diffusion in our systems as the previously described models.

Bond Angle Variation

To evaluate the role of θ_0 on simulated results, we performed a series of simulations with $\theta_0 = 135°$, $k_\theta = 25.0\epsilon/\mathrm{rad}^2$, and $d = 1.0\sigma$ with varying water volume fraction. As shown in Figure S12, at moderate to high water volume fractions, variation of the equilibrium bond angle has almost no effect on simulated diffusivity values. At low water volume fractions,

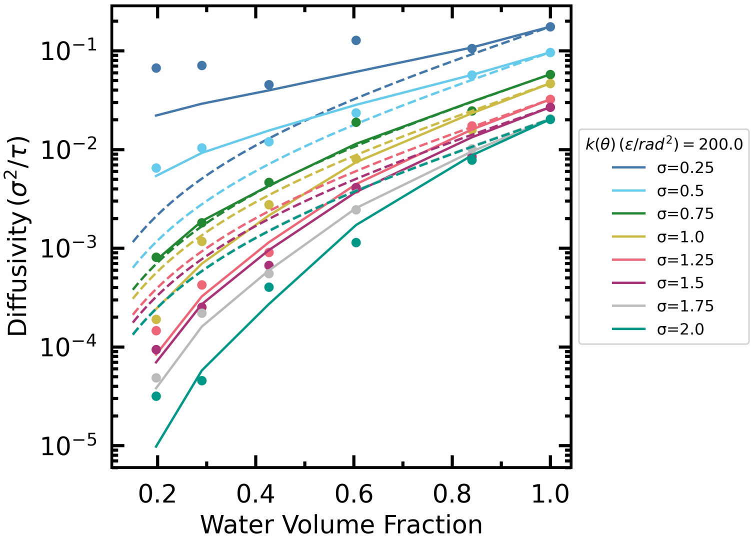

Figure S11: Comparison of simulation data with the Mackie-Meares model (dashed lines) and the modified Mackie-Meares model (solid lines) for $k_\theta = 200.0\epsilon/\text{rad}^2$. We only plot results for the most rigid polymer, due to the assumption that polymer beads are immobile in the Mackie-Meares model.

there appears to be a slight dependence on bond angle, but the overall effect remains small.

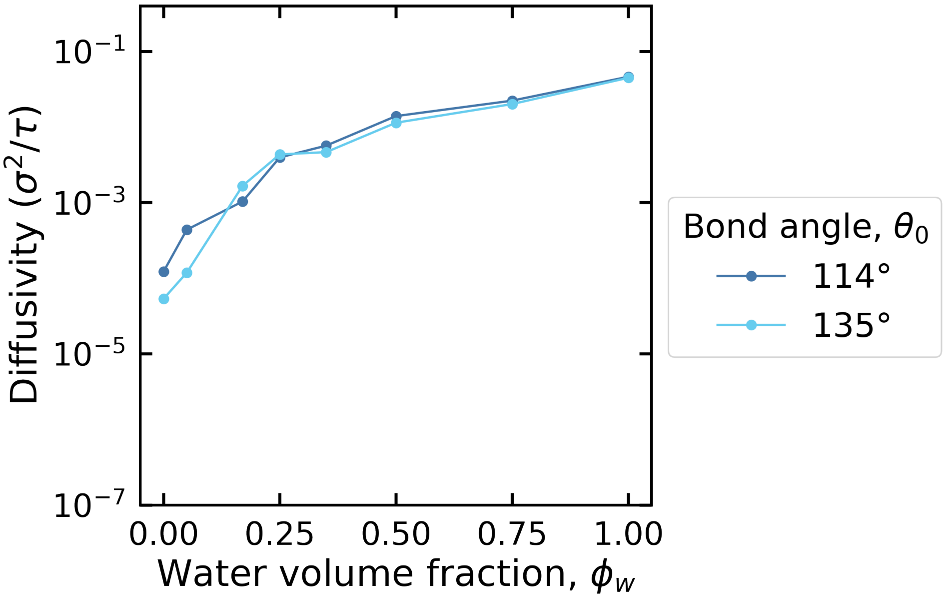

Figure S12: Comparison between $\theta_0 = 114^\circ$ and $\theta_0 = 135^\circ$, with $k_\theta = 25.0\epsilon/\mathrm{rad}^2$ and $d = 1.0\sigma$. Simulated diffusivity values are similar for the two equilibrium bond angles.

References

(1) Bekker, H.; Berendsen, H.; Dijkstra, E.; Achterop, S.; Drunen, R.; Spoel, D.; Sijbers, A.; Keegstra, H. In *Physics Computing 92*; Groot, R., Nadrchal, J., Eds.; 1993; p 252–256.

(2) Berendsen, H.; Spoel, D.; Drunen, R. GROMACS: A message-passing parallel molecular dynamics implementation. *Comput. Phys. Commun.* **1995**, *91*, 43–56.

(3) Lindahl, E.; Hess, B.; Spoel, D. GROMACS 3.0: A package for molecular simulation and trajectory analysis. *J. Mol. Model.* **2001**, *7*, 306–317.

(4) Spoel, D.; Lindahl, E.; Hess, B.; Groenhof, G.; Mark, A.; Berendsen, H. GROMACS: Fast, flexible and free. *J. Comp. Chem.* **2005**, *26*, 1701–1718.

(5) Hess, B.; Kutzner, C.; Spoel, D.; Lindahl, E. GROMACS 4: Algorithms for highly efficient, load-balanced, and scalable molecular simulation. *J. Chem. Theory Comput.* **2008**, *4*, 435–447.

(6) Pronk, S.; Páll, S.; Schulz, R.; Larsson, P.; Bjelkmar, P.; Apostolov, R.; Shirts, M.; Smith, J. GROMACS 4.5: A high-throughput and highly parallel open source molecular simulation toolkit. *Bioinformatics* **2013**, *29*, 845–854.

(7) Páll, S.; Abraham, M.; Kutzner, C.; Hess, B.; Lindahl, E. In *Solving software challenges for exascale*; Markidis, S., Laure, E., Eds.; Springer International Publishing Switzerland: London, 2015; p 3–27.

(8) Abraham, M.; Murtola, T.; Schulz, R.; Páll, S.; Smith, J.; Hess, B.; Lindahl, E. GROMACS: High performance molecular simulations through multi-level parallelism from laptops to supercomputers. *SoftwareX* **2015**, *1–2*, 19–25.

(9) Lindahl, E.; Abraham, M.; Hess, B.; van der Spoel, D. GROMACS 2020.5 manual. 2021.

(10) Kozuch, D. J.; Zhang, W.; Milner, S. T. Predicting the Flory-Huggins parameter for polymers with stiffness mismatch from molecular dynamics simulations. *Polymers* **2016**, *8*.

(11) Chen, R.; Poling-Skutvik, R.; P. Howard, M.; Nikoubashman, A.; A. Egorov, S.; C. Conrad, J.; C. Palmer, J. Influence of polymer flexibility on nanoparticle dynamics in semidilute solutions. *Soft Matter* **2019**, *15*, 1260–1268.

(12) Nikoubashman, A.; Milchev, A.; Binder, K. Dynamics of single semiflexible polymers in dilute solution. *J. Chem. Phys.* **2016**, *145*, 234903.

(13) Zhang, K.; Kumar, S. K. Defining the optimal criterion for separating gases using polymeric membranes. *Soft Matter* **2018**, *14*, 9847–9850.

(14) Martin, M. G.; Siepmann, J. I. Transferable potentials for phase equilibria. 1. United-atom description of n-alkanes. *J. Phys. Chem. B* **1998**, *102*, 2569–2577.

(15) Andreev, M.; Chremos, A.; de Pablo, J.; Douglas, J. F. Coarse-grained model of the dynamics of electrolyte solutions. *J. Phys. Chem. B* **2017**, *121*, 8195–8202.

(16) Irving, P. R.; Sam, G.; Rane, S.; Thirumalai, N.; Marioni, N.; Geise, G. M.; Freeman, B. D.; Ganesan, V. Engineering lithium–magnesium selectivity in hydrated polymer membranes through polymer backbone rigidity. *ACS Macro Lett.* **2025**, *14*, 161–168.

(17) Wheatle, B. K.; Lynd, N. A.; Ganesan, V. Effect of polymer polarity on ion transport: A competition between ion aggregation and polymer segmental dynamics. *ACS Macro Lett.* **2018**, *7*, 1149–1154.

(18) Marioni, N.; Nordness, O.; Zhang, Z.; Sujanani, R.; Freeman, B. D.; Segalman, R. A.; Clément, R. J.; Ganesan, V. Ion and water dynamics in the transition from dry to wet conditions in salt-doped PEG. *ACS Macro Lett.* **2024**, *13*, 341–347.

(19) Müller-Plathe, F. Microscopic dynamics in water-swollen poly(vinyl alcohol). *J. Chem. Phys.* **1998**, *108*, 8252–8263.

(20) Sorichetti, V.; Hugouvieux, V.; Kob, W. Determining the mesh size of polymer solutions via the pore size distribution. *Macromolecules* **2020**, *53*, 2568–2581.

(21) Rubinstein, M.; Colby, R. H. *Polymer Physics*; Oxford University Press: Oxford, New York, 2003.

(22) Cohen, M. H.; Turnbull, D. Molecular transport in liquids and glasses. *J. Chem. Phys.* **1959**, *31*, 1164–1169.

(23) Yasuda, H.; Lamaze, C. E.; Peterlin, A. Diffusive and hydraulic permeabilities of water in water-swollen polymer membranes. *J. Polym. Sci. Part A-2: Polym. Phys.* **1971**, *9*, 1117–1131.